Iron oxyhydroxide mineralization on microbial extracellular polysaccharides

Clara S. Chan [a,*], Sirine C. Fakra [b], David C. Edwards [c], David Emerson [d], Jillian F. Banfield [a]

[a] *Dept. of Earth and Planetary Science, University of California, Berkeley, CA 94720, USA*
[b] *Advanced Light Source, Lawrence Berkeley National Laboratory, Berkeley, CA 94720, USA*
[c] *Dept. of Chemistry and Physics, Wesleyan College, Macon, GA 31210, USA*
[d] *Bigelow Laboratory for Ocean Sciences, West Boothbay Harbor, ME 04575, USA*

Abstract

Iron biominerals can form in neutral pH microaerophilic environments where microbes both catalyze iron oxidation and create polymers that localize mineral precipitation. In order to classify the microbial polymers that influence FeOOH mineralogy, we studied the organic and mineral components of biominerals using scanning transmission X-ray microscopy (STXM), micro X-ray fluorescence (μXRF) microscopy, and high-resolution transmission electron microscopy (HRTEM). We focused on iron microbial mat samples from a creek and abandoned mine; these samples are dominated by iron oxyhydroxide-coated structures with sheath, stalk, and filament morphologies. In addition, we characterized the mineralized products of an iron-oxidizing, stalk-forming bacterial culture isolated from the mine. In both natural and cultured samples, microbial polymers were found to be acidic polysaccharides with carboxyl functional groups, strongly spatially correlated with iron oxyhydroxide distribution patterns. Organic fibrils collect FeOOH and control its recrystallization, in some cases resulting in oriented crystals with high aspect ratios. The impact of polymers is particularly pronounced as the materials age. Synthesis experiments designed to mimic the biomineralization processes show that the polysaccharide carboxyl groups bind dissolved iron strongly but release it as mineralization proceeds. Our results suggest that carboxyl groups of acidic polysaccharides are produced by different microorganisms to create a wide range of iron oxyhydroxide biomineral structures. The intimate and potentially long-term association controls the crystal growth, phase, and reactivity of iron oxyhydroxide nanoparticles in natural systems.

1. INTRODUCTION

Iron oxyhydroxides and organic matter are common and highly reactive components of soil and aqueous environments. They often occur together, such as organics adsorbed onto oxyhydroxide surfaces or minerals coating organic fibrils (e.g. Perret et al., 2000; Mavrocordatos and Fortin, 2002). This association affects the charge and stability of both components. Natural organic matter is more resistant to degradation when adsorbed to iron oxides and oxyhydroxides (Keil et al., 1994; Torn et al., 1997; Kaiser and Guggenberger, 2000; Kleber et al., 2005), especially poorly crystalline materials such as ferrihydrite. Organics, such as humics and microbial cell surfaces, can in turn protect ferrihydrite from recrystallization (Kennedy et al., 2004; Schwertmann et al., 2005).

Intimate organic–mineral associations are often the result of bacterial activity. For instance, it has long been recognized that there are important links between microbial exopolymer production and deposition of iron oxides (Ghiorse, 1984). Some iron-oxidizing microbes extrude polymer structures

upon which they deposit the rapidly-precipitating ferric iron byproducts of their metabolism. However, iron oxides and carbon polymers are sources of essential elements for life, and therefore are subject to biologically mediated decomposition. The reduced carbon in polymers is a potential electron donor for microbes, and iron oxides are electron acceptors for iron-reducing microbes. The creation and destruction of mineralized organics can profoundly affect solution geochemistry, since iron oxides and natural organic matter are the most significant sorbents of metals such as lead and uranium and nutrients such as phosphate.

Much information about organic interactions with metals and minerals has been obtained through studies of synthetic organic–mineral composites (e.g. as reviewed in Nesterova et al. (2003)). Multivalent metals bind to polymers, cross-linking strands and forming three-dimensional structures (e.g. Khairou et al., 2002). Polymer fibrils and films have been shown to nucleate and orient FeOOH crystals in laboratory experiments (Tarasevich et al., 1996; Nesterova et al., 2003), and tend to produce nanometer-size, poorly crystalline minerals (Coe et al., 1995; Finotelli et al., 2004). These same processes likely occur in the environment and thus there is a need to relate these laboratory results to natural processes.

We have previously reported evidence that organics promote crystallization of FeOOH in Piquette Mine microbial mats (Chan et al., 2004). Crystal growth by oriented attachment of iron oxyhydroxide nanoparticles in these mats was described by Banfield et al. (2000). In the Piquette microbial mats, bacterial extracellular polysaccharides are associated with high-aspect ratio (~1:1000) nanocrystals of akaganeite (β-FeOOH). We predict that polymer-influenced mineral formation could occur anywhere iron oxyhdroxides form in organic-rich environments. However, prior studies have not sought evidence that polysaccharide-directed mineralization is a general phenomenon in iron microbial mats.

In this study, we compared mineral–organic associations in samples of microbial mats from a mine and a creek, as well as in a culture of a stalk-forming iron-oxidizing bacterium from the mine microbial mat. Synchrotron-based scanning transmission X-ray spectromicroscopy (STXM) enables the study of the minerals and organic functional group chemistry of hydrated samples with high spatial and spectral resolutions (<40 nm and <0.1 eV, respectively). STXM has proven to be a useful tool for studying both organics and metals in biofilms and biominerals, as demonstrated by work on Mn-oxidizing bacteria (Pecher et al., 2003; Toner et al., 2005), microbial calcification (Benzerara et al., 2004, 2006), and river biofilms (Lawrence et al., 2003; Dynes et al., 2006). We performed synthesis experiments to simulate the postulated mineralization pathway, and used STXM-based carbon and iron near edge X-ray absorption fine structure (NEXAFS) spectroscopy to observe the progression of polymer–iron interactions during the course of mineral formation. Results were compared with observations from natural and cultured samples. These experiments were complemented with theoretical calculations of the iron-complexed saccharides at the carbon 1s absorption edge to gain insight into the mechanism of mineral–polymer interactions.

2. METHODS

2.1. Sampling sites and methods

The Piquette Mine is a former Pb–Zn mine (Tennyson, WI) that flooded subsequent to closure in 1968. Orange microbial mats coat the floor and occur as meter-scale formations on and near the tunnel walls. *In situ* measurements showed that the water temperature was 10 °C and inside the mat the pH was 6.7 and dissolved oxygen was ⩽1 mg/L (⩽30 μM). A more detailed description of the microbiology, geochemical setting, and sampling techniques will be published separately. The mats in the Contrary Creek wetland, in Virginia, are loosely aggregated, fluffy accumulations of iron oxides that form in association with spring-fed waters with high Fe(II) concentrations. The chemical parameters of the water above the mat were pH 5.8–6.4, 1–6.5 mg/L dissolved oxygen, 30–300 μM Fe, as measured every month over the timespan of a year; a description of the environment and microbiology of the wetland was published by Emerson and Weiss (2004). Detailed voltammetric electrochemical profiles of oxygen and iron gradients in the mat environment can be found in Druschel et al. (2008). The creek microbial mat samples were collected with sterile pipettes and stored in test tubes. All samples were stored at 4 °C until analysis.

2.2. Culturing

Iron-oxidizing microbes were cultured using the gradient tube method as described by Emerson and Moyer (1997). Briefly, culture tubes consisted of a FeS–agarose plug on the bottom, covered with a minimal media-0.1% agarose solution bubbled with carbon dioxide until the pH reached ~6–6.5. These tubes were inoculated with 5–10 μl of Piquette Mine microbial mat sample, and then tubes exhibiting growth were selected for serial dilution in order to enrich for iron-oxidizers. Resulting cultures were highly enriched in a stalk-forming iron-oxidizer related to *Gallionella*, as determined by 16S rRNA gene cloning and sequencing, but a pure isolate was not obtained. Samples for TEM analysis were grown in culture tubes prepared in a manner similar to the gradient tube method but without agarose (i.e. liquid gradient tubes).

2.3. Synthesis

The information about the polymer functional group chemistry gained in our previous study (Chan et al., 2004) and current study was used to design synthesis experiments. We chose alginate, a well-characterized acidic microbial polysaccharide, as a template for mineralization. Iron was added to the alginate as dissolved ferric chloride, in an $Fe:COO^-$ molar ratio of ~1:100. The excess of alginate carboxylic groups was used in order to prevent the acidic $FeCl_3$ solution from decreasing the pH of the mixture below the pK_a of alginate (~3.5), ensuring the presence of free carboxylic acid groups to bind with iron, as would be the case in circumneutral environments. No additional buffer was used in order to prevent other Fe phases from precip-

itating (e.g. phosphate) and to keep the organic components of the system to a minimum, thus simplifying interpretation of C 1s NEXAFS spectra. The iron–alginate suspensions were incubated in a shaker at 37 °C (to accelerate mineralization), and samples were taken at various time intervals. Samples were rinsed with deionized water to remove excess alginate (that had not bound Fe) prior to imaging and spectroscopic analysis.

2.4. Electron microscopy

Samples for TEM analysis were mounted directly onto formvar-coated copper grids. These were rinsed with deionized water to prevent salt precipitation, air-dried, and coated with carbon. Samples were examined on a Philips CM200 transmission electron microscope operated at an accelerating voltage of 200 kV, equipped with a GATAN image filtering system and Link ultrathin-window energy dispersive X-ray (EDX) detector.

2.5. Scanning transmission X-ray microscopy (STXM)

For STXM analysis, ~1 μl of sample suspension was deposited onto either a single 100 nm thick Si_3N_4 window (Silson Ltd.) or sandwiched between two windows (to maintain a hydrated environment). STXM measurements were performed on the Molecular Environmental Sciences beamline 11.0.2 (80–2000 eV) and beamline 5.3.2 (250–600 eV) of the Advanced Light Source (ALS) at Lawrence Berkeley National Lab, Berkeley, CA (Kilcoyne et al., 2003). These microscopes use a Fresnel zone plate lens to focus a monochromatic X-ray beam onto the sample. Imaging contrast relies on core electron excitation by soft X-ray absorption (Kirz et al., 1995). The sample is scanned through the fixed beam and transmitted photons are detected via a scintillator–photomultiplier detector assembly to provide 2D images of the sample volume probed. The theoretical spatial and spectral resolution during our measurements were 40 nm and ±0.1 eV, respectively, and all samples were analyzed at ambient temperature and ⩽1 atm He.

Transmission images at energies below and at the relevant absorption edge energies were converted into optical density images (O.D. $= \ln(I_0/I)$ where I_0 is the incident photon flux and I is the transmitted flux). Carbon and iron distribution maps were obtained by taking the difference between optical density images obtained just below and above the relevant absorption edge (280 and 300 eV for carbon, 700 and 709.5 eV for iron). Image sequences (also called "stacks") acquired at multiple energies spanning the relevant absorption edge (280–310 eV for C 1s edge and 700–735 eV for Fe 2p edges) were used to extract NEXAFS spectra. Stack images were aligned via a spatial cross-correlation analysis and NEXAFS spectra were extracted from groups of pixels from regions of interest using the IDL package aXis2000. Clean areas of the silicon nitride membrane were used for normalization of the transmission signal obtained from the areas of interest. Spectra shown in Figs. 5–7 were acquired on air-dried samples. Spectra shown in Fig. 8 were acquired on hydrated samples. Dried samples were used for simplicity once it was confirmed that air-drying did not affect the spectroscopic results. To ensure that our data are representative, many areas of each sample were imaged, and stacks were acquired on at least two equivalents areas of the samples. The "cell" standard shown in Fig. 7d was obtained from a cell of the iron-oxidizing microbe *Mariprofundus ferroxydans*.

We used the bend magnet beamline 5.3.2 STXM optimized for polymer studies, to perform carbon spectromicroscopy. The energy was calibrated at the C1s edge using the 3p Rydberg peak of gaseous CO_2 at 292.74 and 294.96 eV. Beam-induced damage was carefully checked by recording fast stacks using few energy points spanning the C 1s energy range and then a full stack with finer energy resolution on a similar region. We used the same strategy at the MES undulator beamline 11.0.2 for recording Fe 2p absorption spectra using small slit sizes to limit the incident flux ($<10^7$ photons/s) and minimize potential distortion of NEXAFS spectra due to non-linear response of the detector at exceeding flux. No visible alteration of the spectra was observed under those conditions. The energy was calibrated at Fe 2p using the main Fe $2p_{3/2}$ peak of ferrihydrite set at 709.5 eV.

STXM analysis of the samples in transmission mode complements our previous measurements using photo-electron emission microscopy (PEEM), a surface-sensitive technique (Chan et al., 2004). STXM images are similar in appearance to low-resolution TEM images, allowing for correlation of STXM and TEM observations.

2.6. μXRF elemental mapping

Micro X-ray fluorescence elemental mapping was performed at ALS beamline 10.3.2 (Marcus et al., 2004). Samples deposited on silicon nitride windows were mounted on an XYZ stage oriented 45° to the incident beam. Elemental maps were collected using a 5×5 μm beam at 10 keV using a 5×5 μm pixel size, and a dwell time of 150 ms per pixel. X-ray fluorescence counts were collected for K, Ca, Ti, Cr, Mn, Fe, and Zn using a seven-element Ge solid-state detector. Maps were deadtime corrected and processed using the LabView custom software available at the beamline.

2.7. C 1s NEXAFS spectra modeling

The geometry optimized gas phase structures of the constituent monosaccharides of alginate, guluronic and mannuronic acid, and the Fe(guluronate)$(H_2O)_4^{+2}$ complex were obtained with Spartan (Wavefunction, Inc., 2004) using the HF/6-31G* level of theory. The details of the spectral calculations can be found in Edwards and Myneni (2005). Briefly, the optimized structures were input into StoBe (Hermann et al., 2002) to compute a NEXAFS spectrum at the carbon 1s edge for each calculated structure. The theoretical spectra were calibrated using the ΔKohn-Sham approach (Triguero et al., 1999) and analyzed with the software package Molden (Schaftenaar and Noordik, 2000).

3. RESULTS

3.1. Electron microscopy observations of morphologies and mineralogy

3.1.1. Environmental samples

The Piquette Mine microbial mats exhibit the typical structures associated with neutrophilic, microaerophilic iron-oxidizing bacteria, including sheaths reminiscent of the Fe-oxidizing bacterium *Leptothrix ochracea* and twisted stalks reminiscent of the Fe-oxidizing bacterium *Gallionella ferruginea* (Fig. 1a and b). The Contrary Creek mats resemble the Piquette Mine mats in that they contain abundant mineralized sheaths and stalks (Fig. 1c and d). However, the Contrary Creek mats contain structures with other morphologies, such as thin (~0.4 μm wide) twisted stalks (Fig. 1c) as well as stalks of loosely aggregated filaments that resemble braided sticks (Fig. 1d). The Contrary Creek site differs from the oligotrophic Piquette Mine in that it contains more exogenous organic matter due to its association with a wetland. The greater availability of organics and other nutrients may explain the higher diversity of morphotypes.

Both Piquette and Contrary Creek mats contain abundant clusters of filaments that cling to, and sometimes surround, the sheaths and stalks. TEM images of the Piquette Mine filaments (Fig. 2a and b) show that they occur in a variety of widths, but are all composed of thin, nanometers-wide, microns long akaganeite core surrounded by ferrihydrite. The Contrary Creek filaments exhibit a very similar structural arrangement (Fig. 2c and d), with a core of oriented crystals surrounded by a cloud of ferrihydrite. These oriented crystals exhibit 0.31 nm lattice fringe spacings parallel and perpendicular to the filament, consistent with spacings previously observed in the Piquette Mine fil-

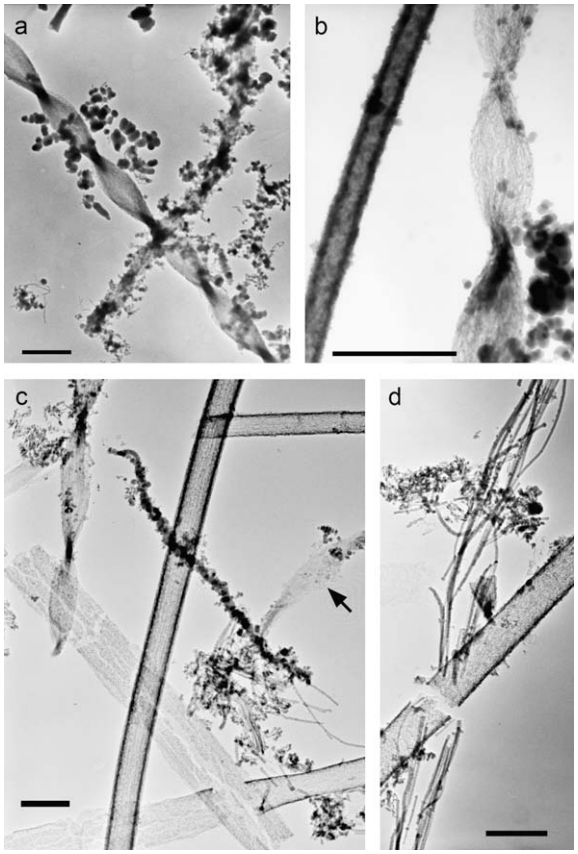

Fig. 1. TEM images of (a, b) Piquette Mine and (c, d) Contrary Creek microbial mat samples showing a variety of morphologies: (a) *Gallionella*-like twisted stalks, colloidal aggregates and thin filaments, (b) thin sheath and twisted stalk (c) *Leptothrix*-like sheaths (including two broken and degraded sheaths), *Gallionella*-like twisted stalks, thin filaments, colloidal aggregates, and a thin twisted stalk; (arrow indicates area of detail show in Fig. 3a), (d) stalk of loosely aggregated filaments ("sticks") and sheath. (all bars = 2 μm).

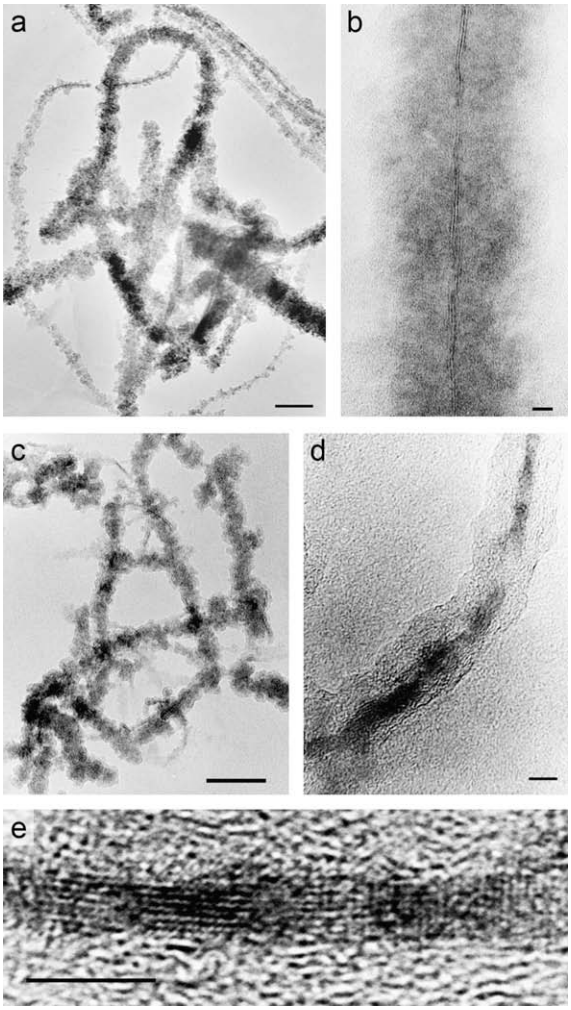

Fig. 2. TEM images of mineralized filaments in (a, b) Piquette Mine and (c, d, e) Contrary Creek microbial mat samples, showing clusters of filaments and filament internal structure with a core of akaganeite surrounded by ferrihydrite. (b) HRTEM image showing 0.75 nm (101) lattice fringes parallel to filament length. (d) Contrary Creek filament showing filament with less symmetry. (e) [−331] zone axis HRTEM image of Contrary Creek filament core showing 0.31 nm horizontal and vertical lattice fringes. (a, c: bars = 100 nm; b, d, e: bars = 5 nm).

ament cores (Chan et al., 2004). However, since the diagnostic 0.7 nm spacings of akaganeite have not been observed, goethite cannot be ruled out. The Contrary Creek filaments differ from the Piquette filaments in that the cores are not always in the center of the filament.

In the Contrary Creek mat sample, some of the twisted stalks appear to be composed of networks of mineralized filaments with oriented crystals. The edge of the stalk shown in Fig. 3a is frayed, and covered in ~3 nm wide, ~100+ nm long oriented crystals of FeOOH. Other stalks contained more densely packed, smaller fibrils covered in abundant crystals of akaganeite, identified by the characteristic 0.7 nm lattice fringe spacings parallel to the length of the fibrils (Fig. 3b). These long filamentous minerals have not been observed in the Piquette mat twisted stalks, which are generally covered in small, round, randomly-oriented nanoparticles of ferrihydrite. We also observe that some

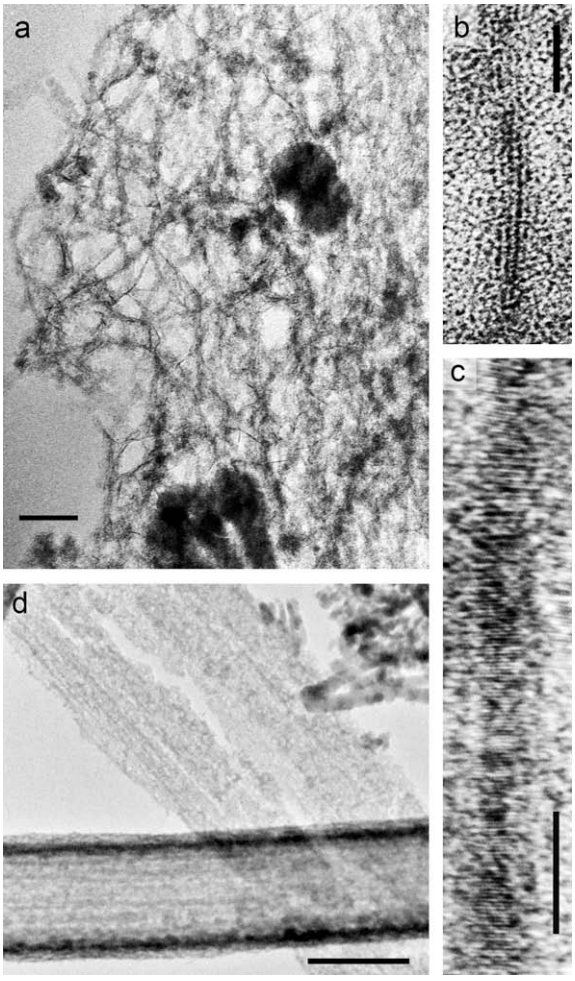

Fig. 3. TEM images of mineralized polymers within structures. (a) frayed edge of Contrary Creek stalk comprised of mineralized filaments (bar = 100 nm), (b) HRTEM image of stalk filament showing 0.7 nm (101) lattice fringes parallel to filament length (bar = 5 nm), (c) HRTEM image of stalk filament showing elongated FeOOH crystals (bar = 5 nm), (d) Intact and broken *Leptothrix* sheaths showing lineations parallel to sheath (bar = 1 μm).

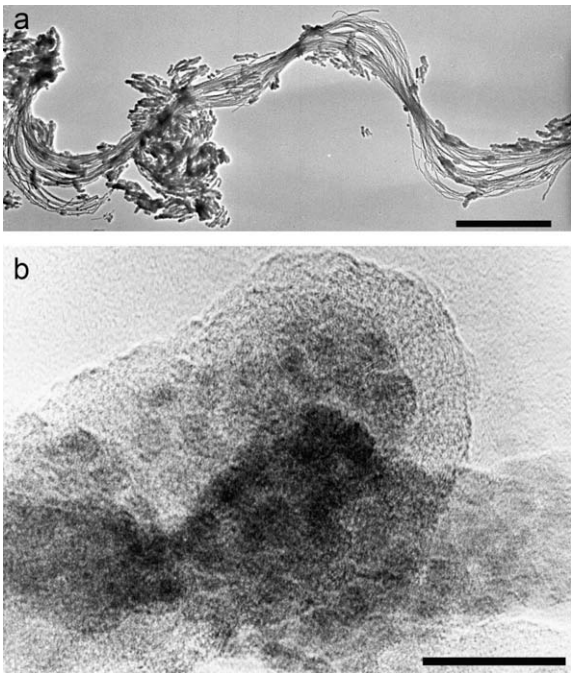

Fig. 4. (a) TEM image of *Gallionella* culture stalk (bar = 2 μm), (b) HRTEM image of ferrihydrite clusters on stalk fibril (bar = 20 nm).

of the Contrary Creek mat sheaths show linear structures parallel to their lengths (long axis), which seem to be more pronounced in older, broken sheaths (Fig. 3d). These have not been examined at high resolution, but could also harbor templated FeOOH minerals.

3.1.2. Cultured microbes

An enrichment culture from the Piquette Mine contains a stalk-forming Fe-oxidizing bacterium that shares 94% 16S rRNA gene sequence identity (Chan, 2006) to previously described *G. ferruginea* (Hallbeck et al., 1993). The twisted stalks are composed of 20 or more loosely associated filaments (Fig. 4a). Each filament is about 20 nm wide and covered in ~5 nm wide spherical clumps of ferrihydrite (Fig. 4b), as determined by electron diffraction (electronic annex Fig. EA-1-1). This stalk structure is similar to that observed by Vatter and Wolfe (1956) in their cultures of *Gallionella*, but differs from the solid ribbon-like stalk morphology observed in the microbial mats from the mine (Fig. 1a).

3.2. Elemental mapping by μXRF and STXM

Micro-X-ray fluorescence maps (Fig. 5) show the distribution of iron, manganese and calcium in the microbial mats. Fig. 5a is a μXRF map of the Piquette Mine microbial mat showing that it is mainly covered in Fe, with Mn and Ca concentrated locally. The iron-rich (red) linear features are the stalks and sheaths. The localized Ca spots could represent cell clusters; they are not likely carbonate particles as no carbonate was detected by C 1s NEXAFS spectroscopy (see below). The localized Mn (shown in

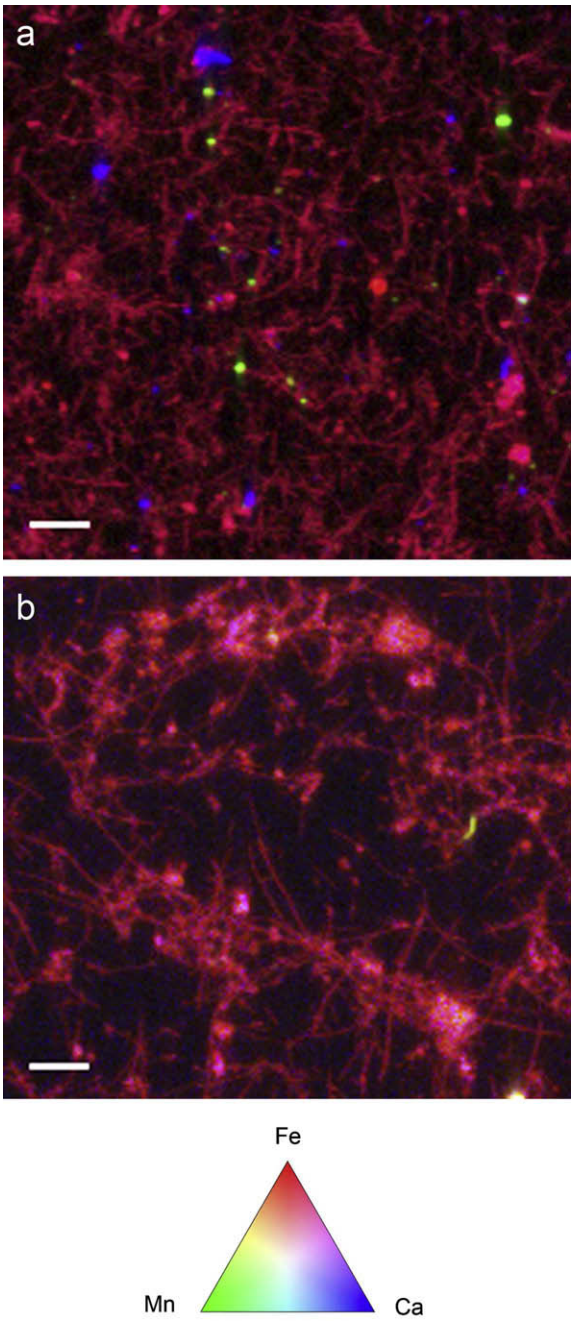

Fig. 5. Tricolor-coded micro X-ray fluorescence (μXRF) elemental maps showing iron (red), manganese (green), and calcium (blue) distribution in (a) Piquette mine microbial mat (5 × 5 μm pixel size), (b) Contrary Creek microbial mat (5 × 5 μm pixel size), (bars = 100 μm).

green) may be due to precipitates formed by manganese-oxidizing bacteria. A μXRF map of Contrary Creek microbial mat sample (Fig. 5b) shows that this mat is similarly covered in iron with small manganese hotspots.

STXM-derived elemental maps show the distribution of C (Fig. 6a and b) and Fe (Fig. 6c and d) in the Piquette Mine and Contrary Creek mat samples. Unlike μXRF elemental maps, in STXM each element is mapped at different times, so while Fig. 6a and c represents the same area of the Piquette Mine mat, the C and Fe maps were obtained from separate but similar areas of the same Contrary Creek mat sample (Fig. 6b and d). Maps of C and Fe show that these elements are co-localized on sheaths, stalks, and filament clusters in the Piquette Mine microbial mat sample (Fig. 6a and c) and in filaments attached to sheaths in two different areas of a Contrary Creek mat (Fig. 6b and d).

3.3. STXM-based NEXAFS spectroscopy

We used STXM to obtain NEXAFS spectra to characterize the composition of representative morphologies observed. Data were collected at the C 1s edge to identify the polymers and at Fe 2p edges to correlate the mineral distribution with carbon.

3.3.1. Carbon NEXAFS spectroscopy

Fig. 7 shows the STXM images at the C edge (300 eV) and C distribution maps for all microbial mat and culture samples analyzed. Fig. 7 also shows C 1s NEXAFS spectra extracted from particular morphologies. None of the spectra resemble the carbonate standard (calcite), with its characteristic peak at 290.3 eV, so from this evidence, and from previous STXM work on carbonate minerals (e.g. Benzerara et al., 2006), we can infer that all of the carbon observed is organic. The stalks, sheaths, and filaments show very similar spectra, with two sharp absorption peaks: one at 286.7 eV and another at values between 288.6 and 288.8 eV. The second peak corresponds well to the 288.8 eV peak of alginate which represents the $\pi^*_{C=O}$ transition associated with the carboxyl group. The intense peak at 286.7 eV is possibly due to ketone or aldehyde functional groups (Myneni, 2002). The spectrum from the alginate standard does have a very small pre-edge peak at 286.7 eV, but this may be a result of contaminants since alginate is purified from natural materials. In the natural samples, the peak at 286.7 eV could be the result of transitions associated with polysaccharide cross-linking, though there is no specific spectral evidence for this in the literature. Another possibility is that some degradation of the polysaccharides has occurred (either in nature or in the microscope) and the peak is due to the aldehyde group of the linear form of the monosaccharides (normally a small fraction of saccharides in solution compared to the ring form) or a derivative of the monosaccharides. The shape and peak positions of the stalk, sheath, and filament C 1s spectra are very similar to one recorded by Benzerara et al. (2004), which was interpreted to represent extracellular polysaccharides.

The chain of circular features in the Contrary Creek sample (designated as "dots" in Fig. 7b) and the clusters in the culture show a distinct spectrum, with peaks around 285.1, 286.7 and 288.2 eV. These resemble spectra from cells covered in extracellular polymers, reflecting the contributions of proteins, polysaccharides, and other organic compounds.

3.3.2. Iron NEXAFS spectroscopy

Fe 2p NEXAFS spectra provide information on the oxidation state of Fe (van Aken and Liebscher, 2002), but cannot be used to discriminate between iron oxyhydroxides

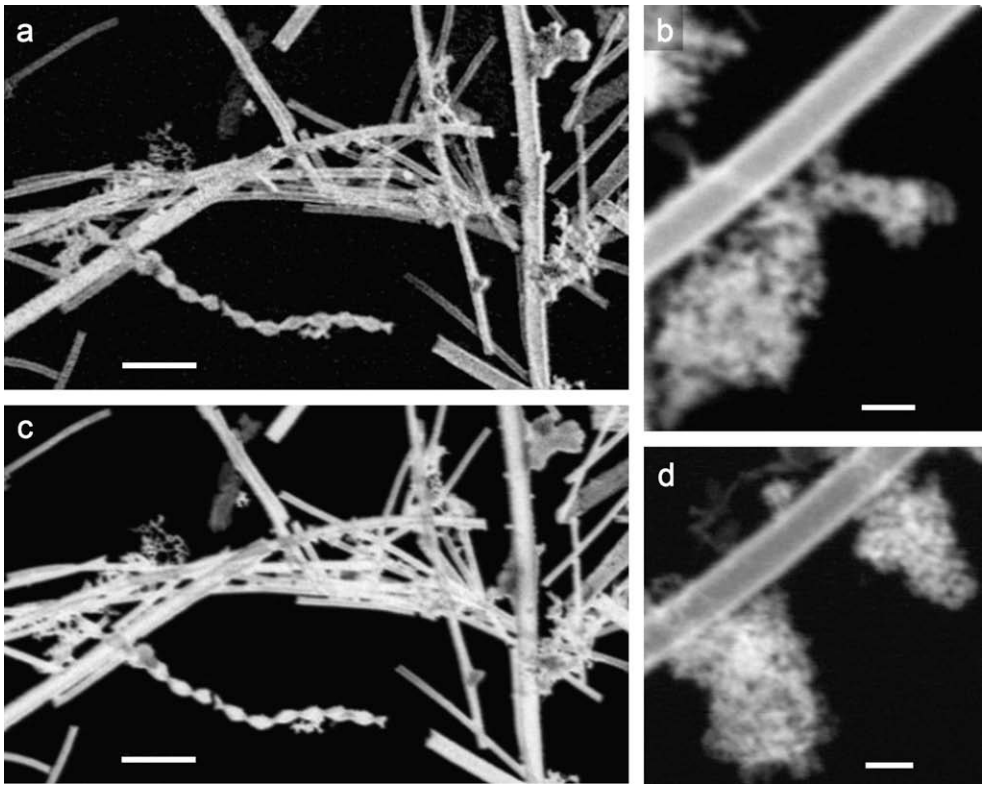

Fig. 6. Pairs of STXM-derived elemental maps showing C–Fe spatial correlation. (a, b) Carbon maps; (c, d) Iron maps, in optical density units. (a) C and (c) Fe distribution maps of a Piquette Mine microbial mat sample (taken in the same region; bars = 5 μm). (b) C and (d) Fe distribution maps of separate, but similar areas in a Contrary Creek mat sample showing filament clusters attached to a sheath (bars = 1 μm). The maximum optical density values are (a) 0.90, (b) 1.25, (c) 2.31, and (d) 2.17.

as their spectra are very similar (electronic annex Fig. EA-1-2). Spectra acquired from the various morphologies in the mat samples show that iron oxyhydroxides are ubiquitous in both natural and cultured samples.

3.4. Synthesis

We analyzed the products of abiotic mineralization experiments in which we combined alginate, a well-characterized microbial polymer with carboxylic functional groups, and $FeCl_3$. As the $FeCl_3$ solution was pipetted into the alginate solution, orange-colored beads about a few millimeters in diameter formed. Over the duration of incubation, these became smaller and more dispersed.

3.4.1. Analysis of synthesis products

The synthesis products appear as clusters of filaments that closely resemble those observed in the natural samples (Fig. 8a). Unlike the natural samples, the filaments were electron beam-sensitive and therefore difficult to image by TEM. STXM images suggest that the filaments grew or aggregated on the timescale of days. We had difficulty obtaining C 1s NEXAFS spectra from the synthetic filaments; because of their small diameter, the carbon concentration approached the instrument detection limit. However, we were able to obtain a spectrum from four day-old filaments (Fig. 8a), and it shows a major peak at 290.0 eV, as well as a smaller pre-edge peak at 286.7 eV. In addition to filaments, the samples contain a "bulk," more gel-like phase, which gave similar, but less noisy spectra. For instance, the filament and bulk spectra (of samples aged 0 and 2 days) both have prominent peaks at ~290 eV (Fig. 8b). Because of the general similarity and better spectral quality, we present the bulk spectra in Fig. 8b.

The C 1s NEXAFS spectra of samples taken immediately after iron addition, and after 2 and 17 days of aging are all distinct (Fig. 8b). The alginate spectrum is shown at the bottom of Fig. 8b for reference, with its major peak at 288.8 eV representing the carboxyl functional group. Upon addition of iron, the 288.8 eV peak disappears and a peak at 290 eV appears. This significant change in the spectrum is interpreted as a result of carboxyl groups binding the iron. After two days, the 290 eV peak is still present but another peak at 288.3 eV appears. At 17 days, the 290 eV peak has disappeared and the spectrum resembles the original alginate spectrum, though the major peak is at 288.5 eV. The reappearance of a peak close in energy to the alginate carboxyl peak is interpreted to be due to free carboxyl groups which are no longer binding iron.

Data obtained at the Fe 2p absorption edges show that these filaments are iron-rich and that iron oxyhydroxides are forming with time. Bulk XRD data show that these iron oxyhydroxides are very poorly crystalline. Taken together, these data show that the interactions between polymer functional groups and iron evolve as iron is bound and then released as mineralization proceeds.

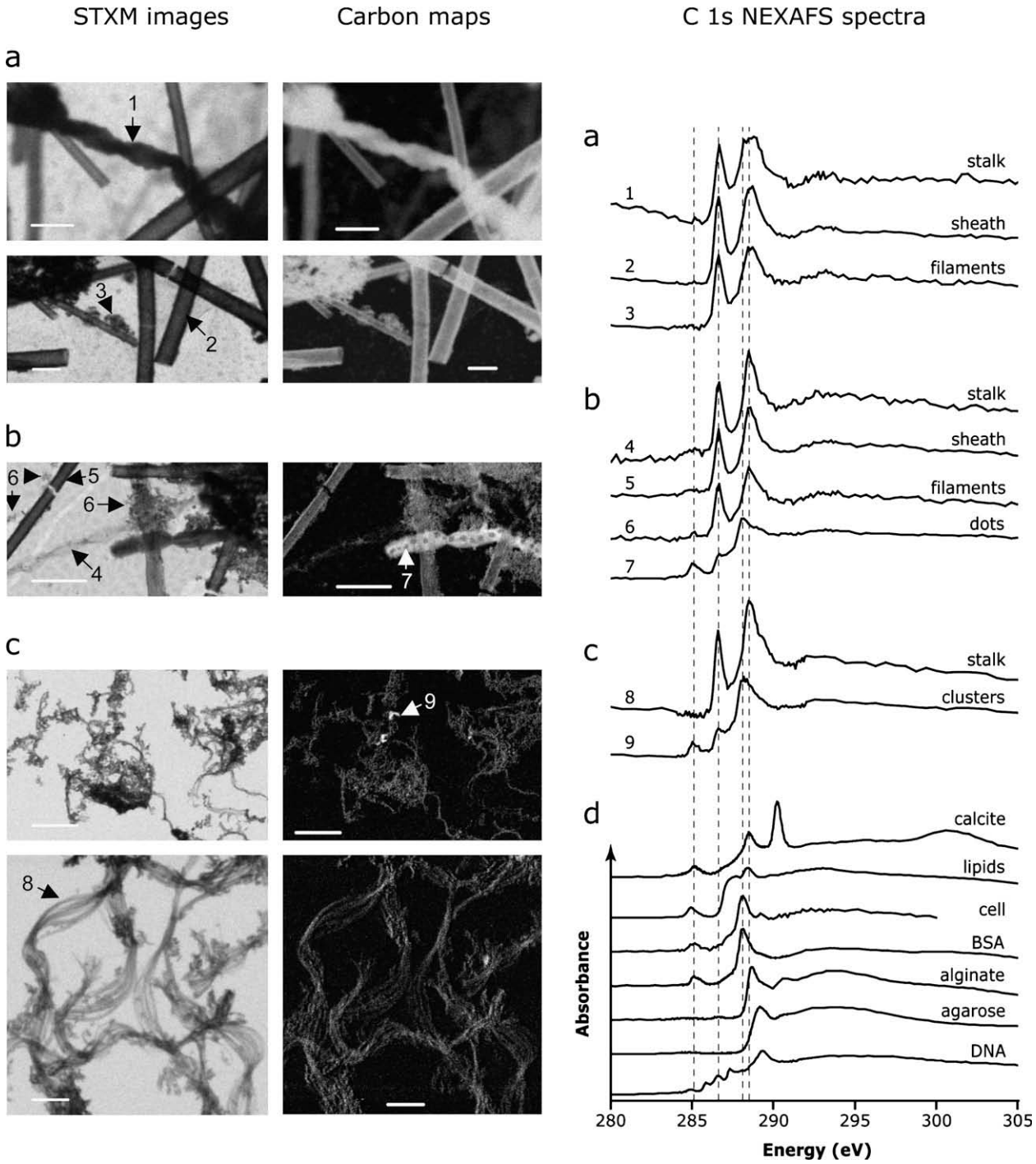

Fig. 7. STXM images (300 eV), carbon distribution maps (in optical density units), and carbon 1s NEXAFS spectra of natural microbial mat and culture samples. (a) Piquette Mine microbial mat (bars = 2 μm), (b) Contrary Creek microbial mat (bars = 5 μm), (c) *Gallionella* culture from Piquette Mine (bars = 10 μm, upper images; 2 μm, lower images), (d) calcite, lipids, microbial cell, bovine serum albumin (BSA) protein, alginate (acidic polysaccharide), agarose (neutral polysaccharide), and DNA standards. Spectra are normalized at 300 eV. The maximum optical density values are (a) 1.23, 1.12, (b) 1.29, (c) 0.87, 0.63. The dashed lines are drawn at 285.2, 286.7, 288.2, and 288.6 eV.

3.4.2. Modeling of alginate–Fe interaction

In order to interpret the C 1s NEXAFS spectra collected from the synthetic samples, we modeled the interactions of ferric iron with alginate. NEXAFS spectra were calculated for alginate (as a combination of mannuronic and guluronic acid, the constituent saccharides of alginate), and alginate plus ferric iron (represented by guluronic acid bound to iron via the carboxylic acid group). The modeled transitions are represented as vertical lines beneath the corresponding experimental spectra in Fig. 8b. Selected orbital and

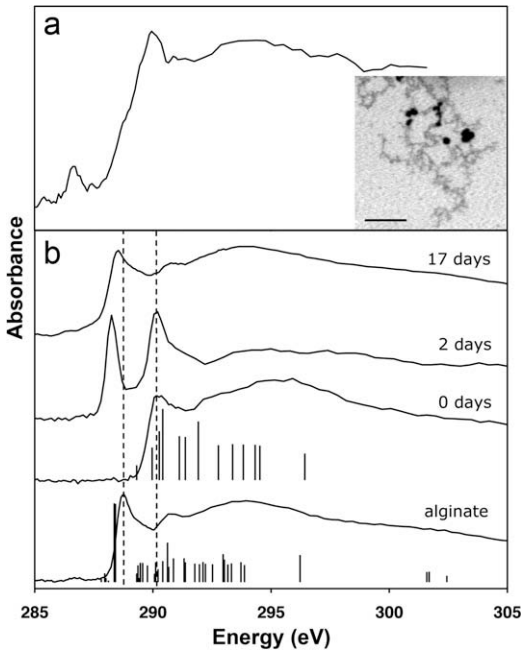

Fig. 8. (a) STXM-based carbon NEXAFS spectrum and image (at 300 eV) of synthetic mineralized filaments sampled 4 days after iron addition to alginate solution. Note major peak at 290.0 eV (bar = 2 μm). (b) STXM-based carbon NEXAFS spectra of alginate and synthetic mineralized filaments sampled immediately after iron addition to the alginate solution, 2 days, and 17 days later. Spectra were normalized at 300 eV. Dashed lines mark the $\pi^*_{C=O}$ transition of carboxylic acid groups (288.5 eV) and the iron-binding carboxyl groups at 290.2 eV. Vertical lines represent modeled transitions (see text for details).

transition structures are shown in electronic annex Figure EA-1-3. The experimental spectrum of alginate is dominated by the carboxyl group $\pi^*_{C=O}$ transition at 288.4 eV, which matches well with the major peak in the experimental alginate spectrum. Small discrepancies in the calculated alginate model may be attributed to small changes that occur when the polysaccharide is in aqueous solution compared to the gas phase. Modeling the alginate complexed to ferric iron shows that the carboxyl group loses π^* character and gains more σ^* character, and the energies of the major transitions shift to 290.3 eV (σ^*_{ring} transition) and 290.6 eV (σ^*_{COO} transition). This shift in bond/orbital character can be explained by the electron donating ability of the polymer to the central iron atom. The shift approximately corresponds to the shift observed in experimental spectra taken before and after ferric iron addition to the alginate, which implies that the absorption peak at 290.5 eV is indicative of iron complexation.

4. DISCUSSION

4.1. Mineralized polymer structure morphologies

In the analysis of natural iron-rich microbial mats and iron-oxidizing microbes in culture, we have observed many variants of stalks, sheaths, and other mineralized structures generally attributed to *Gallionella* and *Leptothrix* species. In order to identify the structure-forming organisms, we attempted to grow them in culture and compare the morphology of iron mineralized-structures with those found in natural microbial mats. We were able to cultivate one stalk-forming species from the Piquette Mine, and confirmed that this organism is a relative of *G. ferruginea*. The stalk produced in culture is different from those observed in environmental samples in that it is a loose aggregation of filaments rather than a solid ribbon. The differences in observed structure morphology between various stalks in nature and between the cultured stalk and natural ones may be due to species-level differences (e.g. *G. ferruginea* vs. *G. filamenta* (Hanert, 1999)). We have shown that the Piquette microbial mat communities contain 5 lineages with 94–96% sequence similarity to *Gallionella* (Chan, 2006), and each of these might produce subtly different stalk types. Alternatively, variation in stalk morphology may be the consequence of growth conditions, extent of mineralization, or degree of aging and decay.

4.2. The iron-binding function of microbial polymers

Although there have been many studies of microbial iron mineralization (e.g. Warren and Ferris, 1998; Chatellier et al., 2001; Glasauer et al., 2001; Mavrocordatos and Fortin, 2002; Chatellier and Fortin, 2004; Rancourt et al., 2005; and other works cited by reviews: Ghiorse, 1984; Konhauser, 1998; Fortin and Langley, 2005; Kappler and Straub, 2005), few provide insight into the mineralization processes of iron-oxidizing microbial cultures and mats. Because of the notable abundance of extracellular polymers in iron microbial mats, we investigated the role of these organics in mineral formation.

In the Piquette Mine and Contrary Creek, iron microbial mats thrive where ferrous iron-rich fluids flow into oxygenated, circumneutral pH waters. As part of their energy metabolism, iron-oxidizers produce ferric iron, which precipitates as iron oxyhydroxides. It is important to note that abiotic oxidation (and mineral formation) rates can outpace biotic oxidation in iron microbial mats (Druschel et al., 2008). In particular, catalysis by oxyhydroxide surfaces can account for a significant portion of oxidation (Rentz et al., 2007; nominally considered "abiotic" though catalysis by biologically-produced minerals might be considered a biotic effect). In all of the samples in this study, acidic polysaccharides were associated with the iron oxyhydroxides, both in organized structures and filament clusters. We infer that cells excrete the carboxyl-rich polymers in order to localize mineral precipitation (both abiotic and biotic). This control over mineralization could confer several advantages to the cells. Not only could it prevent the cells from becoming encrusted in oxyhydroxides, but the cells may also gain an energetic benefit from the localized protons released from mineral formation (Chan et al., 2004; Emerson and Moyer, 1997). In our synthesis experiments, polysaccharide binds ferric iron, and over the course of days to weeks, the iron is released as it polymerizes, ultimately forming iron oxyhydroxides. Thus, we infer that the direct binding of iron by polymers is short term.

4.3. Polymer effects on mineral aging

The microbial mats accumulate over time, and thus contain components of varying ages. For the natural samples analyzed here we do not know the actual age of the material sampled, but we have some time constraints. In the case of the mine, it has been flooded for less than 40 years, although the oxides examined are likely much younger partly due to the fact that the tunnels are subject to flushing during storms. Microbial mats at Contrary Creek are also regularly washed away by rain storms, but have been observed to re-establish themselves within days to weeks. The structures we observe range from less mineralized to more thickly coated, often by more coarsely crystalline minerals, and presumably these latter structures are older. Variation in extent of mineralization is also apparent in the STXM elemental maps, where we observe that some sheaths and stalks contain more iron than others. In TEM images, some structures appear to have partially decayed (e.g. sheaths broken open, frayed stalks fibrils), and we infer that these are older than the intact ones. In general, the structures in the Contrary Creek mat show more evidence of decay and breakage than those from the Piquette Mine. One reason may be that temperatures at Contrary Creek (up to 25 °C in the summer) can be higher than in the Piquette Mine (10 °C year-round), thereby accelerating both decomposition and recrystallization reactions. A perhaps more intriguing explanation is that due to higher organic loading, the Contrary Creek site harbors a more active group of Fe-reducing bacteria, which plays a role in degrading the iron-mineralized structures.

We have observed that very elongate, curved, pseudo-single crystals of akaganeite reported first from the Piquette Mine also occur in filament clusters in a microbial mat at Contrary Creek. Akaganeite also occurs in larger structures such as *Gallionella*-type twisted stalks at Contrary Creek. However, we detected only ferrihydrite on polymers in laboratory cultures of iron-oxidizing bacteria and in laboratory-synthesized iron–polymer composites aged for a few weeks. Although mineralization conditions may not have been identical, the lack of akaganeite in culture and synthesis experiments suggests that polymer-directed recrystallization occurs on a timescale longer than several weeks. Given what is known of the natural sample ages, the actual timescale may be on the order of months.

It has been previously noted that organic polymers induce the formation of the less crystalline iron oxyhydroxides (ferrihydrite), and tend to slow recrystallization to other forms (Kennedy et al., 2004; Schwertmann et al., 2005). Our observations of abundant ferrihydrite in the Piquette Mine mat sample, culture, and synthetic filaments are consistent with this hypothesis. In samples with high organic to iron ratio, Kennedy et al. (2004) attributed the retardation of recrystallization in part to the binding of ferrihydrite to organic functional groups, which constrained the rotation of particles and prevented oriented aggregation. This may explain the lack of akaganeite in the synthetic samples where the organic content was high relative to iron. However, we have shown that oriented aggregation can in fact occur in contact with polymers in the natural samples. In two different microbial mats, and in different structures, FeOOH nanocrystals on natural acidic polysaccharide fibrils are oriented in the same direction relative to the fibril.

In our synthesis experiments, the initial interactions between polymer carboxyl groups and iron were strong. Over time, the carboxyls released iron and FeOOH minerals nucleated. While akaganeite did not form during the course of the experiment, it is possible that it would form over longer timescales. Akaganeite formation would then require a mechanism that entails a weaker interaction than would be involved in templation.

Although we cannot rule out epitaxy in the natural system, there may be alternative explanations for the localized precipitation of akaganeite rather than other forms of FeOOH. For example, polymer-nanoparticle interactions may alter the surface energy, stabilizing akaganeite relative to goethite. In this case, the carboxyl groups in proximity to the surfaces of akaganeite fibers may provide charge balance normally associated with substitution of anions in the channels that parallel the filament length.

5. CONCLUSIONS

We have analyzed two microbial mats and an iron-oxidizing bacterial culture using STXM and TEM. One major advantage of STXM is that samples may be studied in a hydrated state, allowing us to confirm that air-drying did not affect our results. NEXAFS spectroscopic analyses indicate the presence of acidic polysaccharides in close association with iron oxyhydroxides. We also analyzed the minerals on polymers, and observed akaganeite fibers not only in tangled, unordered filaments, but also in organized structures. This work suggests that polymer-directed iron oxyhydroxide mineralization is a general phenomenon that could occur in any system containing acidic polysaccharides and iron.

STXM analyses have shown that both fresh and aged structures contained polysaccharides, so it appears that mineralization also protects the polymers from degradation and contributes to maintaining a long-term carbon pool in these aqueous systems. In turn, the polysaccharides appear to play an important role in determining how the iron oxyhydroxides age. Our results show that recrystallization occurs in the immediate vicinity of polymers, and that these polymers have a direct effect on the mineral products. Such effects do not occur in the short timescales of usual laboratory studies, but such potential long-term changes must be taken into consideration when determining the reactivity and longevity of iron oxyhydroxides associated with organics.

ACKNOWLEDGEMENTS

Funding for this work was provided by University of Wisconsin and National Defense Science and Engineering Graduate fellowships to C.S.C. and by the NASA Astrobiology Institute. The ALS beamlines 11.0.2, 5.3.2 and 10.3.2 and are supported by the Director, Office of Science, Office of Basic Energy Sciences, Division of Materials Sciences and the Division of Chemical Sciences, Geosciences, and Biosciences of the U.S. DOE at LBNL under

Contract No. DE-AC02-05CH11231. We thank D. K. Shuh, T. Tyliszczak, and M. K. Gilles for providing beamtime at BL11.0.2 and A. L. D. Kilcoyne for beamtime at BL5.3.2.

APPENDIX A. SUPPLEMENTARY DATA

Supplementary data associated with this article can be found, in the online version, at doi:10.1016/j.gca.2009.02.036.

REFERENCES

Banfield J. F., Welch S. A., Zhang H., Ebert T. T. and Penn R. L. (2000) Aggregation-based crystal growth and microstructure development in natural iron oxyhydroxide biomineralization products. *Science* **289**, 751.

Benzerara K., Yoon T. H., Tyliszczak T., Constantz B., Spormann A. M. and Brown, Jr., G. E. (2004) Scanning transmission X-ray microscopy study of microbial calcification. *Geobiology* **2**, 249–259.

Benzerara K., Menguy N., Lopez-Garcia P., Yoon T.-H., Kazmierczak J., Tyliszcak T., Guyot F. and Brown G. E. (2006) Nanoscale detection of organic signatures in carbonate microbialites. *PNAS* **103**, 9440–9445.

Chan C. S. (2006) The geomicrobiology of iron-oxidizing microbes. Ph. D. Thesis, University of California, Berkeley.

Chan C. S., De Stasio G., Welch S. A., Girasole M., Frazer B. H., Nesterova M. V., Fakra S. and Banfield J. F. (2004) Microbial polysaccharides template assembly of nanocrystal fibers. *Science* **303**, 1656–1658.

Chatellier X., Fortin D., West M. M., Leppard G. G. and Ferris F. G. (2001) Effect of the presence of bacterial surfaces during the synthesis of Fe oxides by oxidation of ferrous ions. *Eur. J. Mineral.* **13**, 705–714.

Chatellier X. and Fortin D. (2004) Adsorption of ferrous ions onto Bacillus subtilis cells. *Chem. Geol.* **212**, 209–228.

Coe E. M., Bereman R. D. and Monte W. T. (1995) An investigation into the size of an iron dextran complex. *J. Inorg. Biochem.* **60**, 149–153.

Druschel G., Emerson D., Sutka R., Suchecki P. and Luther G. W. (2008) Low-oxygen and chemical kinetic constraints on the geochemical niche of neutrophilic iron(II) oxidizing microorganisms. *Geochim. Cosmochim. Acta* **72**, 3358–3370.

Dynes J. J., Tyliszczak T., Araki T., Lawrence J. R., Swerhone G. D. W., Leppard G. G. and Hitchcock A. P. (2006) Speciation and quantitative mapping of metal species in microbial biofilms using scanning transmission X-ray microscopy. *Environ. Sci. Technol.* **40**, 1556–1565.

Edwards D. C. and Myneni S. C. B. (2005) Hard and soft X-ray absorption spectroscopic investigation of aqueous Fe(III)-hydroxamate siderophore complexes. *J. Phys. Chem. A* **109**, 10249–10256.

Emerson D. and Moyer C. (1997) Isolation and characterization of novel iron-oxidizing bacteria that grow at circumneutral pH. *Appl. Environ. Microbiol.* **63**, 4784–4792.

Emerson D. and Weiss J. V. (2004) Bacterial iron oxidation in circumneutral freshwater habitats: findings from the field and the laboratory. *Geomicrobiol. J.* **21**, 405–414.

Finotelli P. V., Morales M. A., Rocha-Leao M. H., Baggio-Saitovitch E. M. and Rossi A. M. (2004) Magnetic studies of iron(III) nanoparticles in alginate polymer for drug delivery applications. *Mater. Sci. Eng. C-Biomimetic Supramol. Syst.* **24**, 625–629.

Fortin D. and Langley S. (2005) Formation and occurrence of biogenic iron-rich minerals. *Earth Sci. Rev.* **72**, 1–19.

Ghiorse W. C. (1984) Biology of iron- and manganese-depositing bacteria. *Ann. Rev. Microbiol.* **38**, 515–550.

Glasauer S., Langley S. and Beveridge T. J. (2001) Sorption of Fe (hydr)oxides to the surface of *Shewanella putrefaciens*: cell-bound fine-grained minerals are not always formed de novo. *Appl. Environ. Microbiol.* **67**, 5544–5550.

Hallbeck L., Stahl F. and Pedersen K. (1993) Phylogeny and phenotypic characterization of the stalk-forming and iron-oxidizing bacterium *Gallionella ferruginea*. *J. Gen. Microbiol.* **139**, 1531–1535.

Hanert H. H. (1999) The genus *Gallionella*. In *The Prokaryotes: An Evolving Electronic Resource for the Microbiological Community* (ed. M. Dworkin et al.). Springer-Verlag, New York.

Hermann K., Pettersson L. G. M. and Casida M. E. et al. (2002) StoBe-deMon; deMon Software, version 1.0.

Kaiser K. and Guggenberger G. (2000) The role of DOM sorption to mineral surfaces in the preservation of organic matter in soils. *Org. Geochem.* **31**, 711–725.

Kappler A. and Straub K. L. (2005) Geomicrobiological cycling of iron. *Rev. Mineral. Geochem.* **59**, 85–108.

Keil R. G., Montlucon D. B., Prahl F. G. and Hedges J. I. (1994) Sorptive preservation of labile organic-matter in marine-sediments. *Nature* **370**, 549–552.

Kennedy C. B., Scott S. D. and Ferris F. G. (2004) Hydrothermal phase stabilization of 2-line ferrihydrite by bacteria. *Chem. Geol.* **212**, 269–277.

Khairou K. S., Al-Gethami W. M. and Hassan R. M. (2002) Kinetics and mechanism of sol–gel transformation between sodium alginate polyelectrolyte and some heavy divalent metal ions with formation of capillary structure polymembranes ionotropic gels. *J. Membr. Sci.* **209**, 445–456.

Kilcoyne A. L. D., Tyliszczak T., Steele W. F., Fakra S., Hitchcock P., Franck K., Anderson E., Harteneck B., Rightor E. G., Mitchell G. E., Hitchcock A. P., Yang L., Warwick T. and Ade H. (2003) Interferometer-controlled scanning transmission X-ray microscopes at the Advanced Light Source. *J. Synchrot. Radiat.* **10**, 125–136.

Kirz J., Jacobsen C. and Howells M. (1995) Soft X-ray microscopes and their biological applications. *Quarter. Rev. Biophys.* **28**, 33–130.

Kleber M., Mikutta R., Torn M. S. and Jahn R. (2005) Poorly crystalline mineral phases protect organic matter in acid subsoil horizons. *Eur. J. Soil Sci.* **56**, 717–725.

Konhauser K. O. (1998) Diversity of bacterial iron mineralization. *Earth Sci. Rev.* **43**, 91–121.

Lawrence J. R., Swerhone G. D. W., Leppard G. G., Araki T., Zhang X., West M. M. and Hitchcock A. P. (2003) Scanning transmission X-ray, laser scanning, and transmission electron microscopy mapping of the exopolymeric matrix of microbial biofilms. *Appl. Environ. Microbiol.* **69**, 5543–5554.

Marcus M. A., MacDowell A. A., Celestre R., Manceau A., Miller T., Padmore H. A. and Sublett R. E. (2004) Beamline 10.3.2 at ALS: a hard X-ray microprobe for environmental and materials sciences. *J. Synchrotron Rad.* **11**, 239–247.

Mavrocordatos D. and Fortin D. (2002) Quantitative characterization of biotic iron oxides by analytical electron microscopy. *Am. Mineral.* **87**, 940–946.

Myneni S. C. B. (2002) Applications of synchrotron radiation in low temperature geochemistry and environmental science. *Rev. Mineral. Geochem.* **49**, 485–579.

Nesterova M., Moreau J. and Banfield J. F. (2003) Model biomimetic studies of templated growth and assembly of nanocrystalline FeOOH. *Geochim. Cosmochim. Acta* **67**, 1177–1187.

Pecher K., McCubbery D., Kneedler E., Rothe J., Bargar J., Meigs G., Cox L., Nealson K. and Tonner B. (2003) Quantitative charge state analysis of manganese biominerals in aqueous suspension using scanning transmission X-ray microscopy (STXM). *Geochim. Cosmochim. Acta* **67**, 1089–1098.

Perret D., Gaillard J. F., Dominik J. and Atteia O. (2000) The diversity of natural hydrous iron oxides. *Environ. Sci. Technol.* **34**, 3540–3546.

Rancourt D. G., Thibault P. J., Mavrocordatos D. and Lamarche G. (2005) Hydrous ferric oxide precipitation in the presence of nonmetabolizing bacteria: constraints on the mechanism of a biotic effect. *Geochim. Cosmochim. Acta* **69**, 553–577.

Rentz J. A., Kraiya C., Luther G. W. and Emerson D. (2007) Control of ferrous iron oxidation within circumneutral microbial iron mats by cellular activity and autocatalysis. *Environ. Sci. Technol.* **41**, 6084–6089.

Schaftenaar G. and Noordik J. H. (2000) Molden: a pre- and post-processing program for molecular and electronic structures. *J. Comput. Aided Mol. Des.* **14**, 123–134.

Schwertmann U., Wagner F. and Knicker H. (2005) Ferrihydrite-humic associations: magnetic hyperfine interactions. *Soil Sci. Soc. Am. J.* **69**, 1009–1015.

Tarasevich B. J., Rieke P. C. and Liu J. (1996) Nucleation and growth of oriented ceramic films onto organic interfaces. *Chem. Mat.* **8**, 292–300.

Toner B., Fakra S., Villalobos M., Warwick T. and Sposito G. (2005) Spatially resolved characterization of biogenic manganese oxide production within a bacterial biofilm. *Appl. Environ. Microbiol.* **71**, 1300–1310.

Torn M. S., Trumbore S. E., Chadwick O. A., Vitousek P. M. and Hendricks D. M. (1997) Mineral control of soil organic carbon storage and turnover. *Nature* **389**, 170–173.

Triguero L., Plashkevych O., Pettersson L. G. M. and Agren H. (1999) Separate state vs. Transition state Kohn-Sham calculations of X-ray photoelectron binding energies and chemical shifts. *J. Electron Spectrosc. Relat. Phenom.* **104**, 195–207.

van Aken P. A. and Liebscher B. (2002) Quantification of ferrous/ferric ratios in minerals: new evaluation schemes of Fe L_{23} electron energy-loss near-edge spectra. *Phys. Chem. Miner.* **29**, 188–200.

Vatter A. E. and Wolfe R. S. (1956) Electron microscopy of *Gallionella ferruginea*. *J. Bacteriol.* **72**, 248–252.

Warren L. A. and Ferris F. G. (1998) Continuum between sorption and precipitation of Fe(III) on microbial surfaces. *Environ. Sci. Technol.* **32**, 2331–2337.